ELSEVIER

Journal of Fluids and Structures 24 (2008) 1098–1119

JOURNAL OF FLUIDS AND STRUCTURES

www.elsevier.com/locate/jfs

Interaction between a submerged evacuated cylindrical shell and a shock wave—Part II: Numerical aspects of the solution

S. Iakovlev

Department of Engineering Mathematics and Internetworking, Dalhousie University, Halifax, NS, Canada B3J 2X4

Received 27 June 2006; accepted 28 January 2008
Available online 10 April 2008

Abstract

The interaction between a submerged elastic circular cylindrical shell and an external shock wave is addressed. A linear, two-dimensional formulation of the problem is considered. A semi-analytical solution is obtained using a combination of the classical analytical approach based on the use of the Laplace transform and separation of variables, and finite difference methodology. The study consists of two parts. Part I focuses on the simulation and analysis of the acoustic fields induced during the interaction. Both the diffraction (absolutely rigid cylinder) and complete diffraction–radiation (elastic shell) are considered. Special attention is paid to the lower-magnitude shell-induced waves representing radiation by the elastic waves circumnavigating the shell. The focus of Part II is on the numerical analysis of the solution. The convergence of the series solution and finite-difference scheme is analysed. The computation of the response functions of the problem is discussed as well, as is the effect of the bending stiffness on the acoustic field. The membrane model of the shell is considered to analyse such effect, which, in combination with the models addressed in Part I, allows for the analysis of the evolution of the acoustic field around the structure as its elastic properties change from an absolutely rigid cylinder to a membrane. The results of the numerical simulations are compared to available experimental data, and a good agreement is observed.

1. Introduction

The second part of the present study addresses various issues arising when one uses the solution developed in the first part to simulate the interaction. The following aspects are considered: the one-dimensional benchmark plots of the quantities of interest, numerical analysis of the solution (the study of the series convergence and that of the finite-difference scheme), analysis of the effect of the bending stiffness on the acoustic field, and computing the response functions of the problem. Unless stated otherwise, all the parameters of the system are the same as in Part I: we consider a steel shell with the thickness-to-radius ratio 0.01 submerged into water and subjected to a step-exponential cylindrical incident wave with $p_\alpha = 250\,\text{kPa}$, $\lambda = 0.0001314\,\text{s}$, and the stand-off $S_R = 4r_0$.

E-mail address: serguei.iakovlev@dal.ca

0889-9746/$ - see front matter © 2008 Elsevier Ltd. All rights reserved.
doi:10.1016/j.jfluidstructs.2008.01.005

Nomenclature

c_f	sound speed in the fluid, $\hat{c}_f = 1$
c_s	sound speed in the shell material, $\hat{c}_s = c_s c_f^{-1}$
h_0	thickness of the shell, $\hat{h}_0 = h_0 r_0^{-1}$
I_n	modified Bessel function of the first kind of order n
K_n	modified Bessel function of the second kind of order n
k_0^2	coefficient in the shell equations
N	number of terms considered in truncated series
p_α	peak incident pressure, $\hat{p}_\alpha = p_\alpha \rho_f^{-1} c_f^{-2}$
p	total pressure in the fluid, $\hat{p} = p \rho_f^{-1} c_f^{-2}$
p_0	incident pressure, $\hat{p}_0 = p_0 \rho_f^{-1} c_f^{-2}$
p_d	diffraction pressure, $\hat{p}_d = p_d \rho_f^{-1} c_f^{-2}$
p_r	radiation pressure, $\hat{p}_r = p_r \rho_f^{-1} c_f^{-2}$
r	radial coordinate of the polar coordinate system, $r = \varrho r_0^{-1}$
r_0	radius of the shell, $\hat{r}_0 = 1$
S_R	incident shock wave stand-off, $\hat{S}_R = S_R r_0^{-1}$
t	time, $t = \tau c_f r_0^{-1}$
v^*	transverse displacement of the middle surface of the shell, $v = v^* r_0^{-1}$
w^*	normal displacement of the middle surface of the shell, $w = w^* r_0^{-1}$
ε	strain in the middle surface of the shell
θ	angular coordinate of the polar coordinate system
λ	exponential decay rate, $\hat{\lambda} = \lambda c_f r_0^{-1}$
ξ_n^e	'volume' response functions
ρ_f	density of the fluid, $\rho_f = 1$
ρ_s	density of the shell material, $\hat{\rho}_s = \rho_s \rho_f^{-1}$
ϱ	radial coordinate of the polar coordinate system, $r = \varrho r_0^{-1}$
τ	time, $t = \tau c_f r_0^{-1}$
ψ_n^e	'surface' response functions

$(*)_n \sin n\theta$ and $(*)_n \cos n\theta$ denote the harmonics of (*). Unless stated otherwise, capitalized symbols denote the Laplace transforms of the corresponding functions. Other symbols are defined in the text

2. One-dimensional benchmark plots

The purpose of this section is to provide easy-to-read data for the pressure, displacement, and strain that could be used as a benchmark for verification of numerical results, or for preliminary estimates of the hydrodynamic loads and structural response. For the reasons discussed in Appendix of Part I, the interaction with a plane step-exponential incident wave is considered here (the parameters λ and p_α are the same as before). We note that for the purposes of numerical code verification, the complexity of the loading hardly makes any difference, at least when the two possibilities are a cylindrical and plane waves. Furthermore, the author felt that since the present work is largely based on the ideas introduced in Geers (1969), it was appropriate to use the same incident load as in that work in at least some parts of the present study. We also note that to make the graphs included as useful as possible, the following dimensionless form of the variables is used: pressures (Figs. 1 and 2) are normalized to the peak incident pressure (i.e. p/p_α is plotted), displacements (Fig. 3) are normalized to the shell thickness (w/h_0 is shown), and strains (Fig. 4) are dimensionless by definition.

We emphasize that, unlike in figure 5 of Part I, all the quantities in this section are plotted exactly as they are produced by the series solution, i.e. no effort has been made to filter out the low-magnitude high-frequency 'noise' seen in some of the plots, not even in the regions where the respective functions are known to be zero from the physical considerations. Such an approach was chosen to illustrate the limitations of the solution obtained here, especially when it comes to simulating pressure. From the practical point of view, however, the decision to retain the numerical noise should not have any effect on the usefulness of the graphs since the regions of zero pressure are always easy to identify when the acoustic speeds in the fluid and shell are known, and those regions seem to be where the convergence problems are most pronounced. We also note that the pressure is the only function that exhibits such noise even when the number of terms retained in the respective series is significant. The displacements are free of noticeable numerical noise for large N, and almost so are the strains (which exhibit very minor noise in very localized regions).

3. Numerical analysis of the solution

The results discussed in Part I, and especially the one-dimensional graphs presented in the previous section, would not be complete without proper numerical analysis of the solution. Specifically, the convergence of the series describing the solution, as well as that of the finite-difference scheme employed to solve the equations for the displacement harmonics, need to be addressed. Since the same methodology has been used by the author to analyse other scenarios of

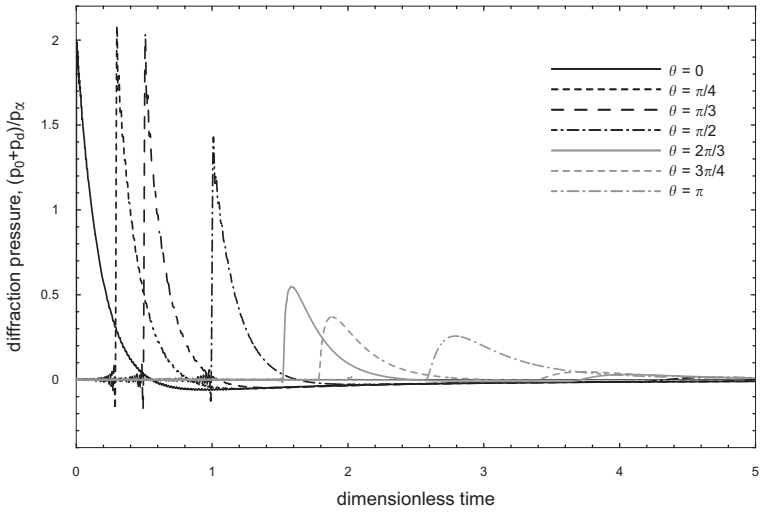

Fig. 1. Time-history of the diffraction pressure.

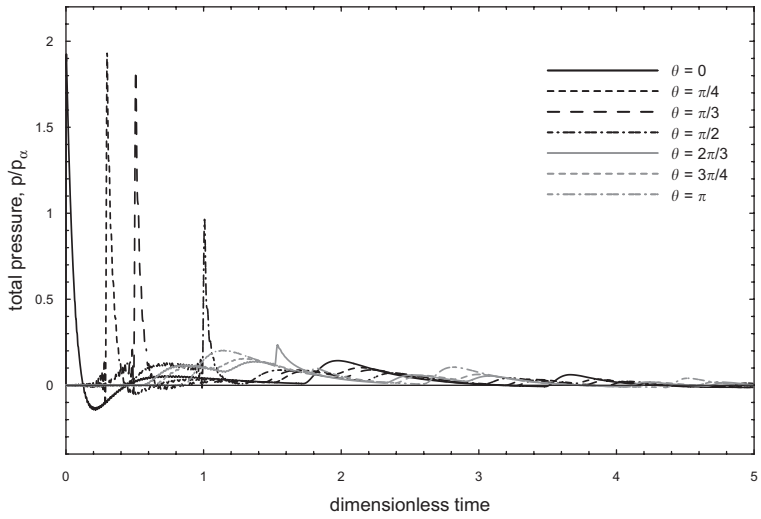

Fig. 2. Time-history of the total diffraction–radiation pressure.

shell–shock interaction [e.g., Iakovlev (2006, 2007)], such numerical analysis will be useful beyond the present work, and will be a good starting point in assessing the accuracy of simulations for a variety of setups, both ones that have already been considered and that are yet to be addressed. We assume the same plane incident wave as in the previous section.

3.1. Series convergence

We start with the analysis of the series convergence. It needs to be analysed separately for pressure, displacements, and strains since the worst converging series will determine the number of terms that will need to be considered throughout the solution (assuming, of course, that all the variables of the system are of interest). We consider the truncated series

$$(*) = \sum_{n=0}^{N} (*)_n \cos n\theta, \tag{1}$$

where $(*)_n \cos n\theta$ are the harmonics of the variable $(*)$, and analyse the error produced by different N. We start the analysis with the surface of the shell, and look at several graphs illustrating how different series converge.

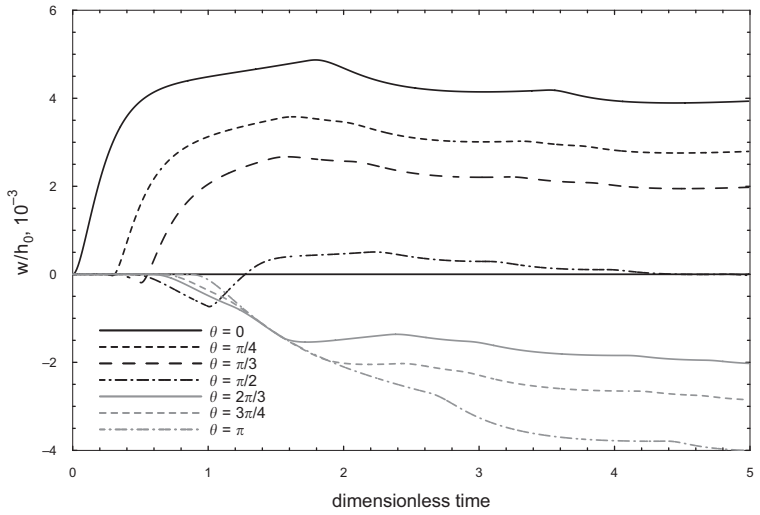

Fig. 3. Time-history of the normal displacement.

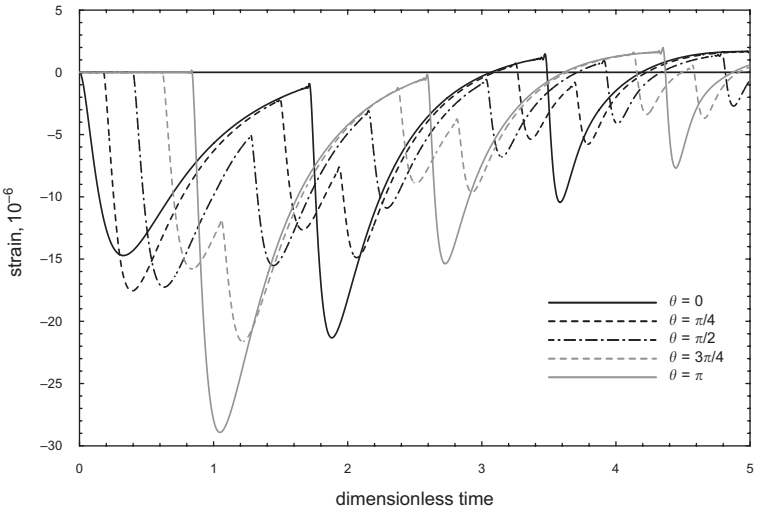

Fig. 4. Time-history of the strain.

Fig. 5 illustrates the convergence of the diffraction pressure at the head point, and Fig. 6 shows a close-up of the 'problem' region near $t = 0$ where the pressure has a discontinuity. It is obvious that the convergence depends on t: although $N = 50$ provides quite a reasonable accuracy for larger t, it is not sufficient in the close proximity of zero. Fig. 7 illustrates the convergence at the tail point. The convergence is particularly easy to analyse in this case since there is an extensive region where the pressure is known to be zero. Again, the convergence strongly depends on t, and is much worse in the 'zero' region where even $N = 300$ results in a noticeable error. The origins on the little non-physical 'bump' at $t = 2$ at the tail point are not clear, but it seems to be a Gibbs-like phenomenon since the magnitude and frequency of the oscillations in the proximity of that point increase with N. We note that the poor convergence in the 'problem' regions can be significantly improved by using convergence improvement techniques, for example, modified Cesaro summation [e.g., Zhang and Geers (1993)].

Figs. 8 and 9 illustrate the convergence of the normal displacement at the head and tail points, respectively. The convergence in this case is evidently better. In particular, even as few as 10 terms provide a very good approximation, and the zero region (tail point) exhibits no noticeable 'noise' when N is large enough. We will see shortly that the displacements indeed are the best converging functions in this problem. Figs. 10 and 11 show the convergence of

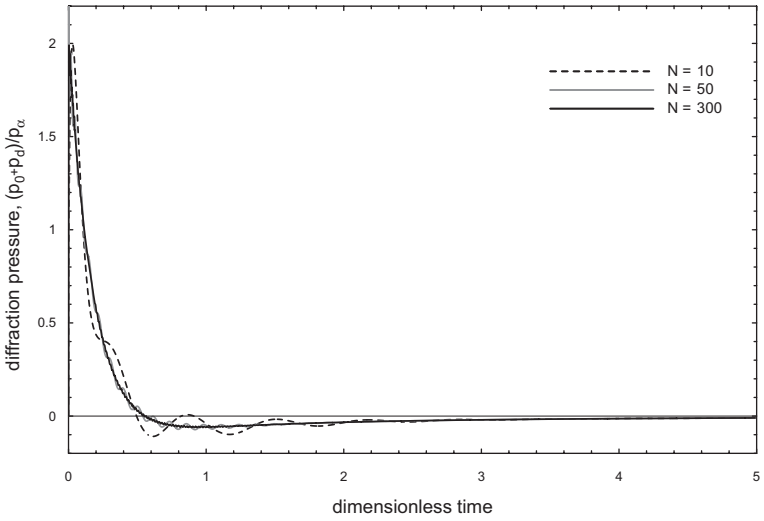

Fig. 5. Convergence of the series for the diffraction pressure, head point.

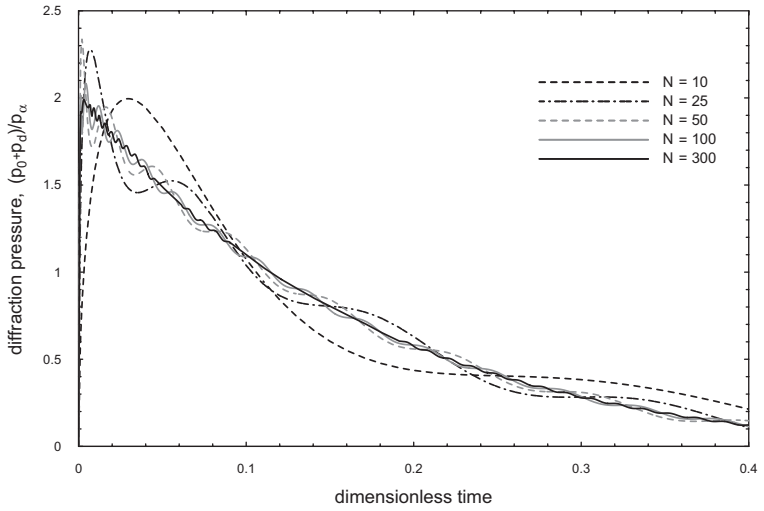

Fig. 6. Convergence of the series for the diffraction pressure at small t, head point.

the strain. Even though the convergence is very good in this case as well, it is not as good as it was for the displacement. The zero region, however, is still free of any noticeable numerical noise for large enough values of N. We note that it is not at all surprising that the stain converges slower than the displacements—because of the derivative θ-wise in Eq. (4) of Part I, the corresponding terms in the respective series are multiplied by n.

Table 1 summarizes the results of the one-dimensional analysis of the series convergence. When estimating the error at the head point, a very close proximity of zero was not taken into account. It was also possible to estimate the error over the 'zero region' at the tail point for $N = 300$ because it was known from the physical considerations where the pressure should be zero. It is particularly obvious now that the pressure series converges much slower than the series describing the strain and normal displacement. Thus, when one is only concerned with the stress–strain state, even as few as 10 terms in the respective series will provide acceptably accurate results. If, however, the acoustic field needs to be analysed (or even the pressure distribution on the shell surface), at least 100 terms need to be kept in the series; even then, problems may arise in certain regions, and convergence improvement techniques may be welcome. We also note that the radiation pressure converges much faster than the diffraction one, and thus the convergence of the total acoustic pressure is determined by that of the diffraction pressure. The normal displacement, strain, and total pressure

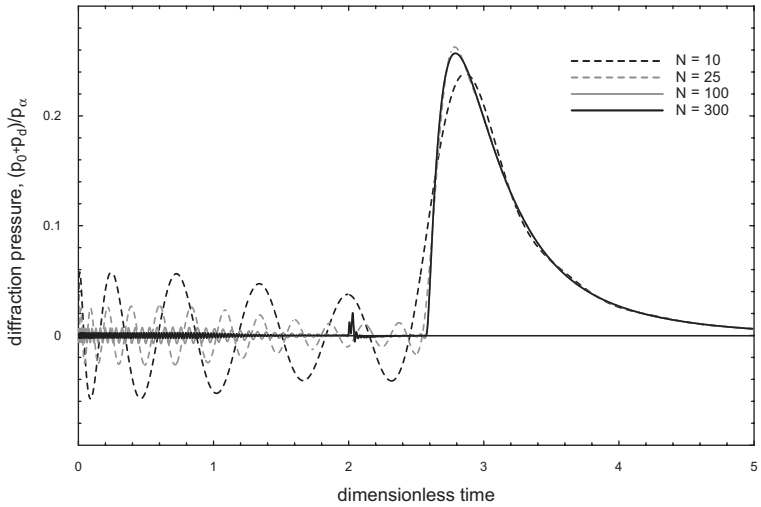

Fig. 7. Convergence of the series for the diffraction pressure, tail point.

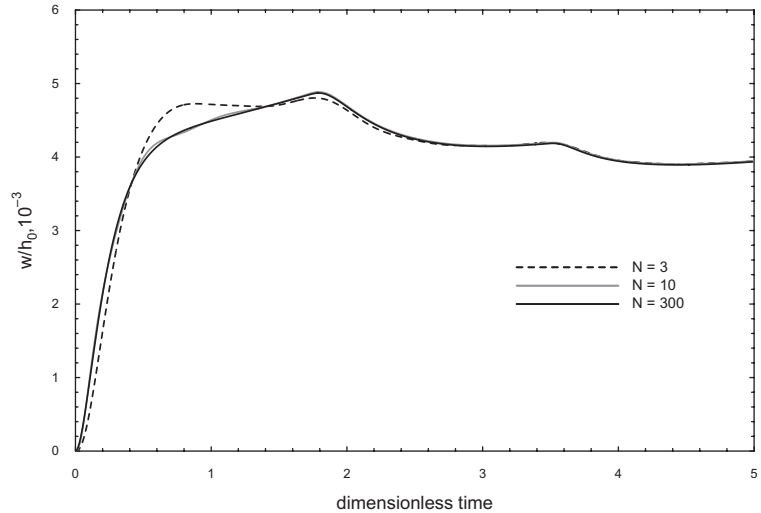

Fig. 8. Convergence of the series for the normal displacement, head point.

appear to exhibit very similar convergence at the head and tail points; the same does not seem to be the case for the diffraction and radiation pressure.

We now turn to the analysis of the series convergence everywhere inside the fluid domain, not only on the shell surface. This, obviously, only applies to the pressure. The instant $t = 2.30$ was chosen to ensure that the shadow zone not yet affected by the diffracted wave is well-represented as well. Fig. 12 shows the diffraction field for four different values of N: 300, 100, 50, and 25. One can see that even for $n = 100$ certain rather obvious non-physical features appear in the plots; for such N, however, they are either very low-magnitude or very localized, and thus do not obscure the wave pattern to any significant degree. We emphasize that these non-physical 'wave features' are very non-uniform in their distribution, and the regions where they are relatively high-magnitude tend to be localized near the wavefront. This is not surprising at all, considering the discontinuity of the pressure at the front and the associated Gibbs phenomenon. As N decreases, the numerical noise becomes more and more pronounced, and at $N = 25$ it very significantly alters the appearance of the acoustic field, and can hardly be called 'noise' anymore.

We would like to emphasize that the relative numerical value of the error due to truncating the series used in simulations is not always representative of how it affects the appearance of the respective two-dimensional fields when

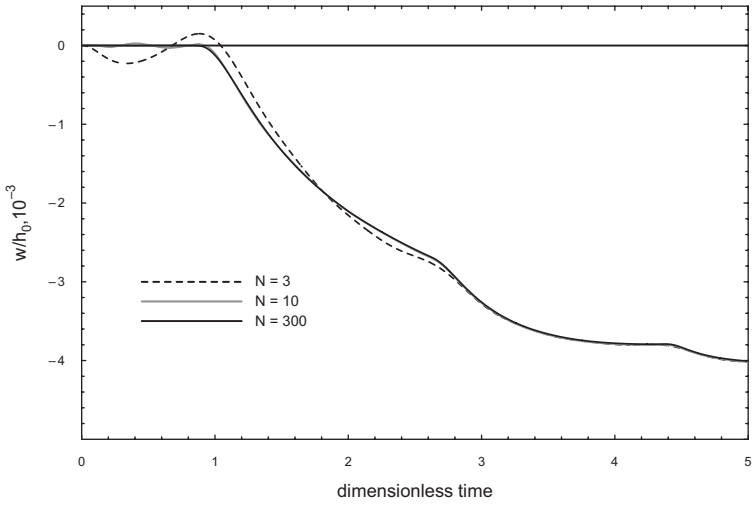

Fig. 9. Convergence of the series for the normal displacement, tail point.

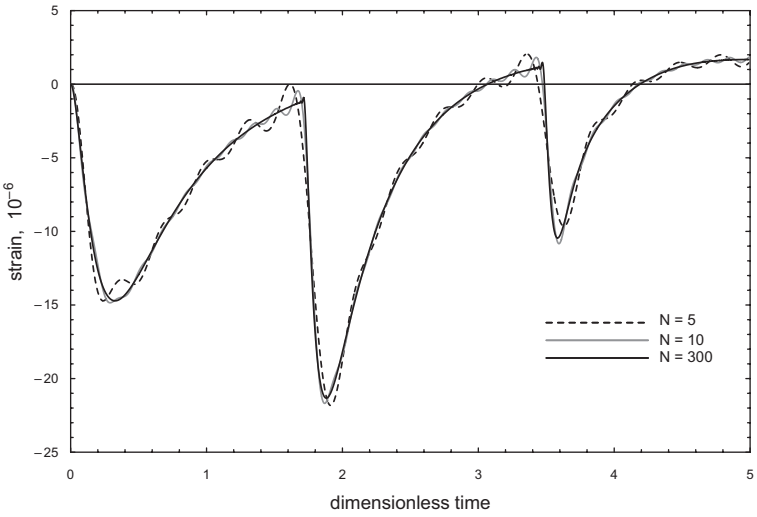

Fig. 10. Convergence of the series for the strain, head point.

they are visualized. For example, consider Fig. 12(b). It is obvious that the pressure pattern is not entirely physically adequate, even in the 'non-problem' regions far behind the wavefront: the symmetric mesh-like 'ripples' clearly indicate that a numerical error of some kind is present in the simulations. At the same time, the maximum magnitude of the ripples in question is less than 1% of the maximum pressure shown, an error which would certainly be considered acceptable in engineering applications. This underlines the importance of distinguishing between the accuracy of simulations sufficient for general analysis, and that required for realistic visualization of two- and three-dimensional fields.

In order to get a better idea of how the series truncation error is distributed in space, we plot the difference between what we regard as the 'converged' solution ($N = 300$) and the fields simulated with $N = 150$, 100, 50, and 25, Fig. 13. It is particularly clear now that the most significant error is observed in the proximity of the incident wavefront, with the second largest error regions localized around the scattered wavefront. Not less importantly, the maximum error is observed inside the fluid domain, far away from the shell surface. Table 2 summarizes the magnitudes (as a percentage of the maximum incident pressure) and locations (r_{max} and θ_{max}) of the maximum absolute error for various N, as well as the magnitudes of the tertiary non-physical 'ripples' discussed earlier. It is particularly clear now that the convergence

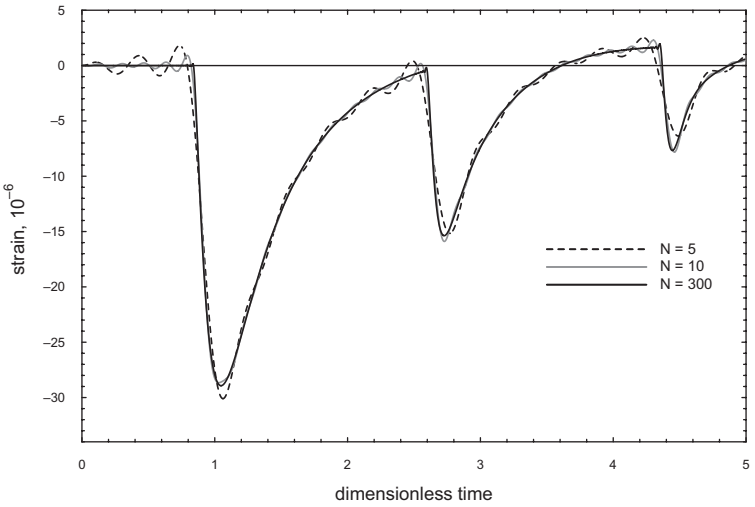

Fig. 11. Convergence of the series for the strain, tail point.

Table 1
Maximum percentage error due to series truncation, the surface of the shell

	N							
	3	5	10	25	50	100	150	300
Diffraction pressure, p_d, head point	–	–	18.9	15.1	7.3	3.7	3.8	–
Diffraction pressure, tail point, zero region	–	–	21.4	10.0	5.3	4.1	4.7	7.6
Diffraction pressure, tail point, non-zero region	–	–	25.3	7.6	2.0	0.58	0.25	–
Radiation pressure, p_r, head point	–	–	10.7	2.7	1.2	0.48	0.31	–
Radiation pressure, tail point, zero region	–	–	17.9	6.8	2.8	1.0	0.5	0.2
Radiation pressure, tail point, non-zero region	–	–	36.7	13.1	4.5	1.3	0.7	–
Total pressure, p, head point	–	–	18.6	14.4	7.2	3.8	3.8	–
Total pressure, tail point	–	–	21.7	10.5	6.2	3.8	3.9	–
Normal displacement, w, head point	10.2	4.7	1.2	0.3	0.15	0.03	0.004	–
Normal displacement, tail point	5.2	2.7	0.7	0.23	0.16	0.04	0.004	–
Strain, ε, head point	29.2	19.1	8.2	1.9	0.6	0.15	0.06	–
Strain, tail point	23.1	14.6	5.9	1.4	0.5	0.12	0.05	–

is not the same throughout the fluid domain, and, therefore, the convergence analysis only performed on the shell surface is of limited use when acoustic fields are of interest.

Summarizing the analysis carried out, it appears that when one intends to accurately visualize the acoustic field around a shock-interacting structure using the present solution, as many as 300 terms need to be kept in the respective series, with $N = 150$ been sufficient if slight imperfections of the field images are acceptable or can be downplayed by the visualization technique used. In the present study, either 150 or 300 terms were considered. If, however, one is only concerned with the stress–strain state, the number of terms required is significantly lower, and even $N = 25$ would ensure very good accuracy, especially for the displacements.

3.2. Finite-difference scheme convergence

There is one more aspect of the solution that needs to be addressed, namely the convergence of the finite-difference scheme, Eqs. (37) and (38) of Part I, adopted to solve the equations for the harmonics of the displacements. Fig. 14 shows the normal velocity at the head point for various step sizes h. We note that even though the equation for the harmonics of the radiation pressure (Eq. (28) of Part I) includes the second derivative of w_n, in the actual computations

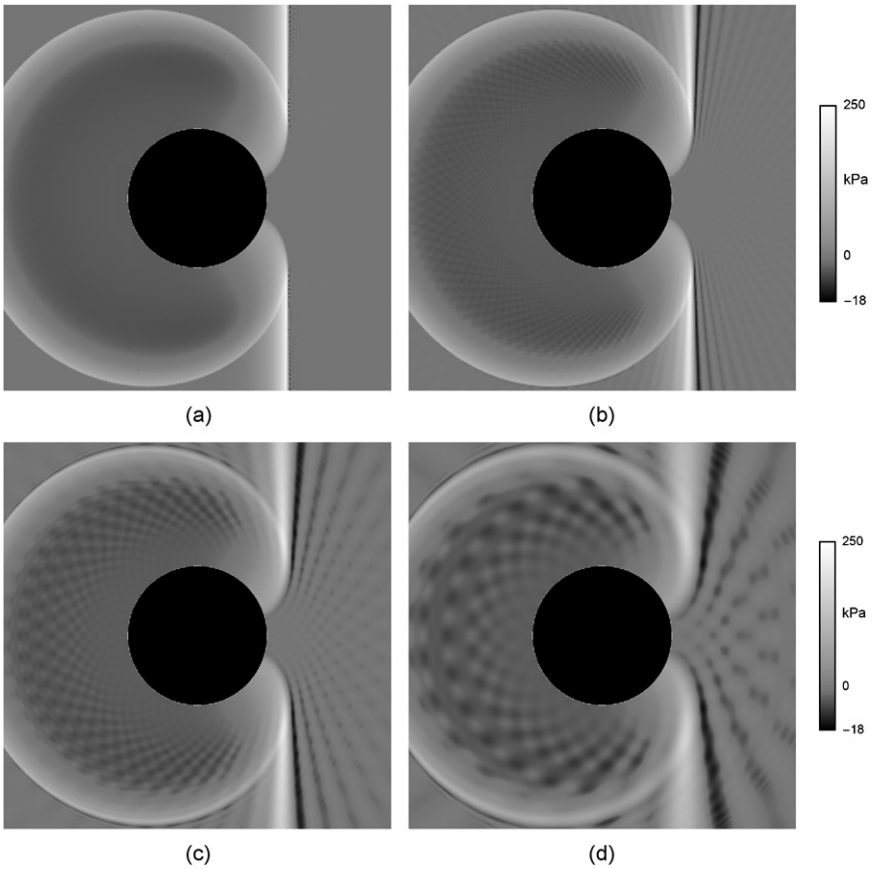

Fig. 12. Diffraction field at $t = 2.30$ for $N = 300$ (a), 100 (b), 50 (c), and 25 (d).

of the radiation pressure a variant of that equation was used where the integrand is the product of the first derivatives of w_n and ξ_n^e. We, therefore, address the normal velocity here.

One can see that twofold decrease of the step size leads to rather significant changes in $\dot{w}$ all the way down to $h = 0.001$. After that, it appears that the scheme has converged since another twofold reduction of h results in a very insignificant (about 1%) change in $\dot{w}$. Thus, the step size in Eqs. (37) and (38) of Part I was chosen to be 0.001. We mention that the results shown in Fig. 14 were produced without bending stiffness. If bending stiffness is taken into account, the scheme diverges for the step size of 0.002 or more in the time interval of interest (for $h = 0.002$ it starts to diverge at $t \approx 1.3$, and for $h = 0.004$ and 0.005 at $t \approx 1$). However, when the step size is reduced to 0.001 or less, the scheme starts to converge rapidly, and the difference between the displacements produced by $h = 0.001$ and 0.0005 is even smaller than in the membrane case (less than 0.5%). Therefore, regardless of the deformation model, the step size of 0.001 appears to provide reasonably accurate results.

4. Effect of bending stiffness

The effect of incorporating the bending stiffness into the shell model (which is equivalent to retaining the terms multiplied by k_0^2 in the shell equations) was discussed in detail in Iakovlev (2007), but the analysis was confined to the shell surface, and the spatial distribution of the contribution of the bending stiffness terms was not addressed. It certainly is of interest to see what the effect of taking the bending stiffness into account is when the entire acoustic field is considered, not only the near-surface region. Moreover, it would definitely be of theoretical interest to compare the acoustic fields under the three distinctly different scenarios of shock-cylinder interaction: a rigid cylinder (figure 2 of Part I), an elastic shell (figure 4 of Part I), and a membrane (Fig. 15 of the present part), and reflect on the evolution of

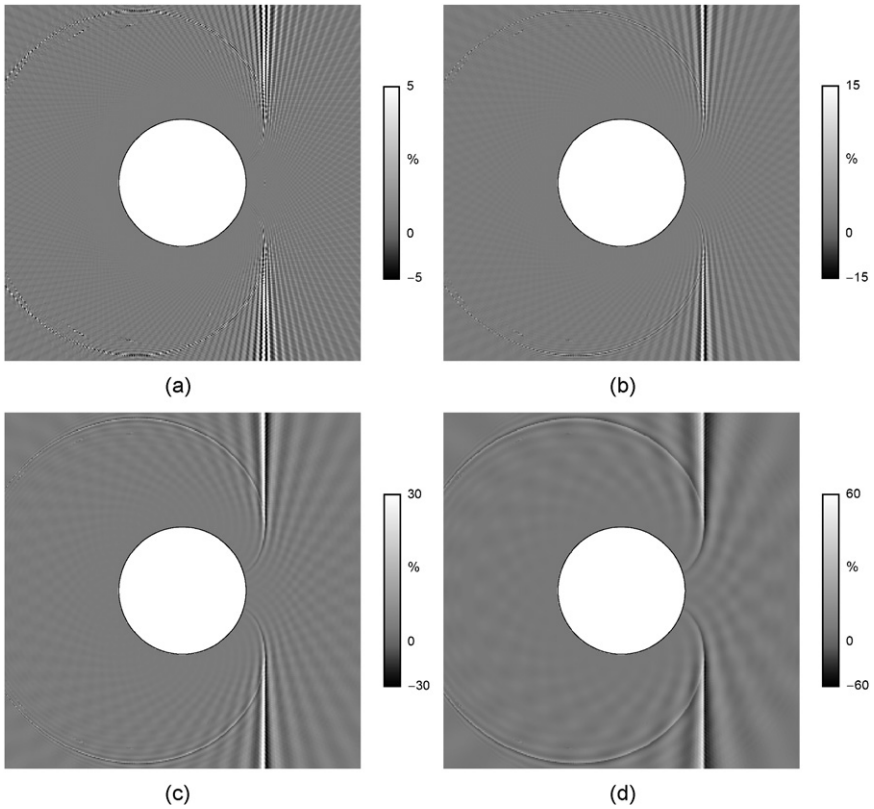

Fig. 13. Difference between the 'converged' ($N = 300$) solution for the diffraction field and the solutions produced by the truncated series with $N = 150$ (a), 100 (b), 50 (c), and 25 (d).

Table 2
Maximum percentage error due to series truncation, the diffraction field

	N			
	25	50	100	150
Maximum error (%)	58	46	31	20
r_{max}	2.88	2.88	3.01	3.01
θ_{max} (°)	−116.4	−116.4	115.2	115.2
Tertiary 'ripple' magnitude (%)	1.8	0.98	0.61	0.37

the total acoustic field as the stiffness of the structure changes from absolutely rigid to membrane state. Here we are back to the cylindrical incident wave described in the introduction.

Fig. 15 shows the total acoustic field around the shell with $h_0/r_0 = 0.01$ when bending stiffness is neglected; the same instants as in figure 4 of Part I (where the bending stiffness is taken into account) are considered. It is apparent that the overall pressure distribution, as well as its magnitude, is very similar in the two cases, to the point of being practically identical. This is consistent with the earlier observations of the surface pressure (Iakovlev, 2007), and further supports the conclusion made about the relative insignificance of retaining the bending stiffness terms when the shell is thin enough ($h_0/r_0 \leqslant 0.01$).

Since the images produced by the membrane and complete elastic models are so similar, we have to look at the sequential plots of the difference between the pressure fields produced by the two models, Fig. 16, to get an idea about what actually changes when we switch from one model to the other. One can see that the noticeable difference is localized in the proximity of the scattered wavefront, has a very high frequency, and that its magnitude is small compared to that of the diffracted–radiated field (the absolute maximum of the difference is about 20% of the

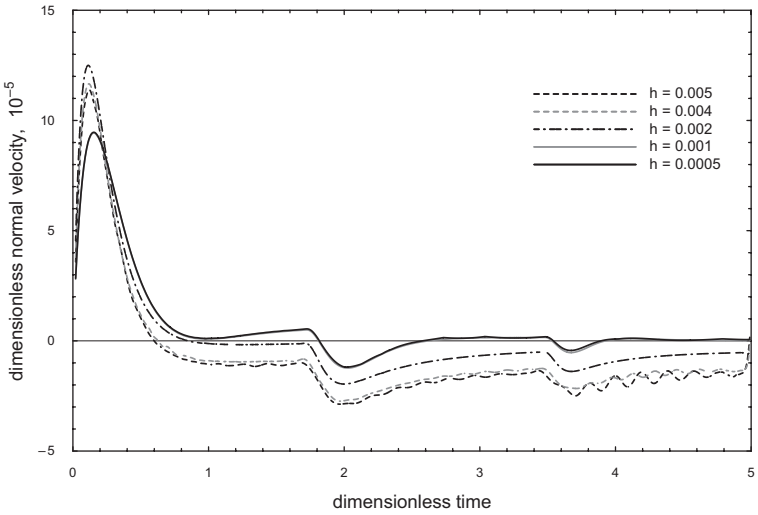

Fig. 14. Convergence of the finite-difference scheme.

maximum incident pressure, and it is attained relatively early in the interaction; a typical maximum magnitude of the difference is less than 10% of the peak incident pressure during the mid-interaction, and it decays to about 5% during the late interaction). Thus, it is not surprising at all that the snapshots in the figure 4 of Part I and Fig. 15 here look so similar. A close-up of the difference, Fig. 17, reveals an extremely low-magnitude component (less than 1% of the peak incident pressure) present during the late interaction. It geometrically corresponds to the upstream propagation of the Mach stems that merge at the tail point at $t \approx 2.74$, compare figure 2 of Part I. Thus, it appears that the bending stiffness only manifests itself in the proximity of the points of contact between the loading (incident or scattered) and the shell, and does not otherwise affect the radiation of the acoustic waves by the shell.

We also look at the difference between the models with and without bending stiffness for a thicker shell, $h_0/r_0 = 0.03$, Fig. 18. One can see that even though the difference is not considerably higher in magnitude than in the $h_0/r_0 = 0.01$ case, the frequency of the oscillations is much lower; more importantly, the difference is much less localized that before. The highest magnitude of the difference is still reached in the proximity of the scattered wavefront, but the zones where the difference is significant are considerably wider than in the $h_0/r_0 = 0.01$ case. Thus, the observation made earlier (Iakovlev, 2007) is further supported: for thicker shells, neglecting the bending stiffness may lead to considerable changes in the acoustic field, and one needs to be very careful making a decision about using the membrane model. We also note that the secondary waves associated with the Mach stems moving upstream now have much higher magnitude (no close-up is necessary to depict them), and, unlike the primary ones, they do not have a clearly defined wavefront. The latter feature is not surprising since the upstream-propagating scattered wave does not have a front either.

There is another important issue that we would like to address here. Namely, it was demonstrated (Iakovlev, 2007) that even though at least two types of waves induced by the elastic processes in the shell are experimentally observed [Ahyi et al. (1998) and Ahyi (2006)], i.e. the S_0 wave (symmetric Lamb wave) and A_0 wave (antisymmetric Lamb, or pseudo-Rayleigh, wave), only one of them, S_0, is reproduced by the membrane model. However, when one compares some of the snapshots illustrating the difference between the complete elastic and membrane models, Fig. 16 and, particularly, Fig. 18, to experimental images, e.g., figure 3 of Part I or Fig. 19 of the present part introduced shortly, it is very tempting to identify the high-frequency wave propagating ahead of the incident wavefront as the pseudo-Rayleigh A_0 wave observed in the experiments. However, to make such identification, we need to simulate the acoustic field for the thickness-to-radius ratios for which experimental data exists [e.g., Ahyi et al. (1998), $h_0/r_0 = 0.06$, $t \approx 1.20$, Fig. 19(a)].

Preliminary analysis indicates that taking the bending stiffness into account for thicker shells leads to a 'mixed' radiated field which is neither the S_0 wave nor the A_0 wave, but a combination of the two without a defined boundary in either geometry or magnitude, Fig. 19(b) (similarly to the experimental image discussed in Part I, SR is the scattered wave, and I is the incident wave). The simulated field also appears to extend beyond the region affected by the waves seen in the experiment. Here, to ensure that the waves of significantly different magnitudes (i.e. the scattered and shell-induced ones) are visible equally well, different pressure ranges were used in different regions of the simulated image. As a result, the image, as far as the pressure magnitudes are concerned, is not a completely realistic representation of the actual acoustic field; that, however, is not a concern in the present case since we are mostly interested in the geometry of the waves, not their

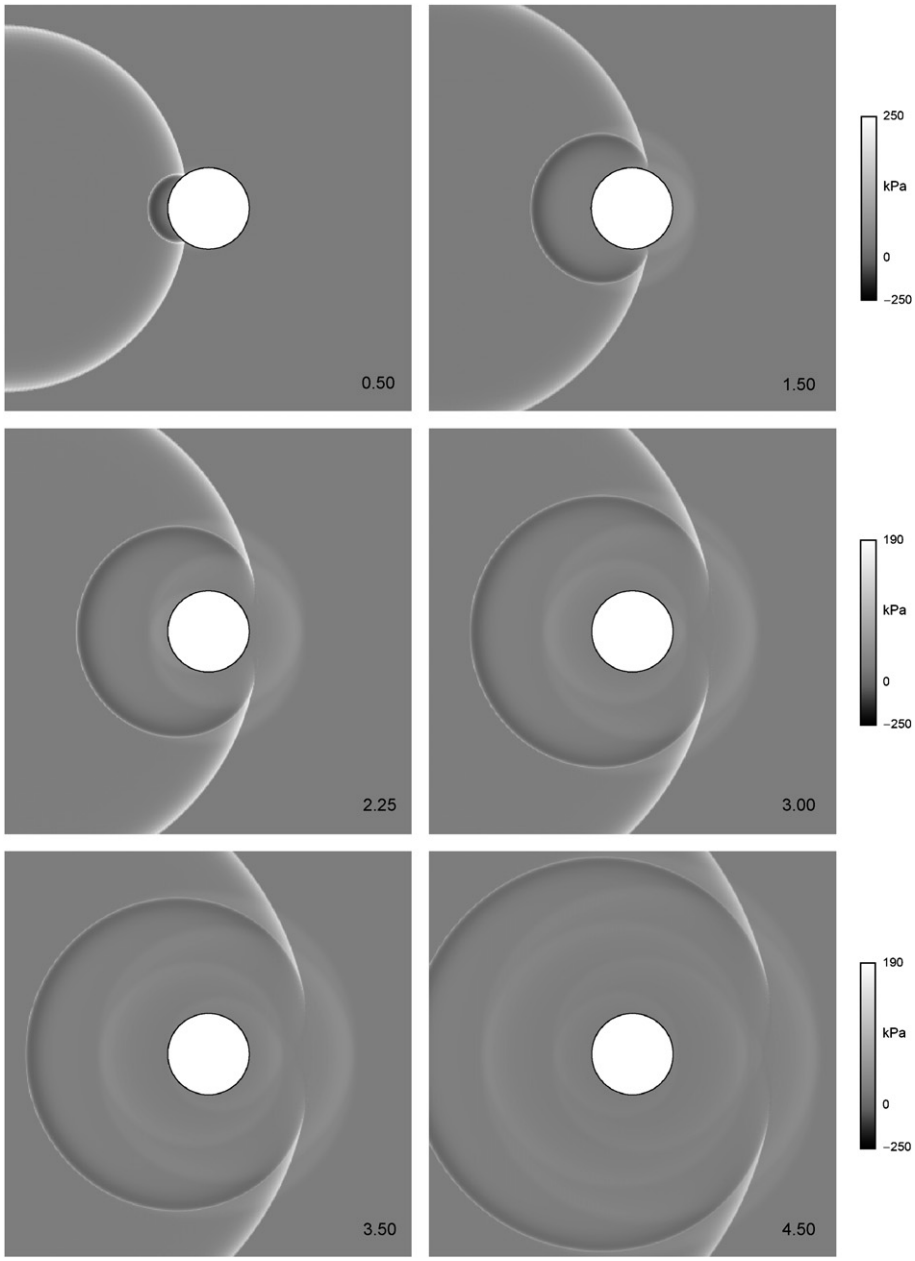

Fig. 15. Dynamics of the complete diffracted–radiated field around an empty submerged shell, membrane model, $h_0/r_0 = 0.01$.

magnitude. For the same reason, the pressure legend is not displayed either. The mixed simulated wave pattern observed is certainly of interest, and further investigation of the issue is definitely needed. However, the author feels that it is beyond the scope of this work, and that, due to the theoretical importance of such a study, it needs to be carried out separately, preferably incorporating all the existing results for the radiation (both stationary and transient) by an elastic shell.

What does, however, appear to be reasonable to include in this work, is a simpler study aimed at simulating the radiated field for a thicker shell using the membrane model and comparing the results with the experiments. Fig. 20(a) shows such simulation for a shell with $h_0/r_0 = 0.06$ (again, the halftones here were assigned differently for different thicknesses and in different regions of the images, so the pressure legends are not shown). One can see that of the two distinctly different shell-radiated waves observed in the experiment, only one (S_0) is reproduced in the numerical simulations. Unlike the results produced by the complete elastic model, however, the geometry of the simulated S_0 wave

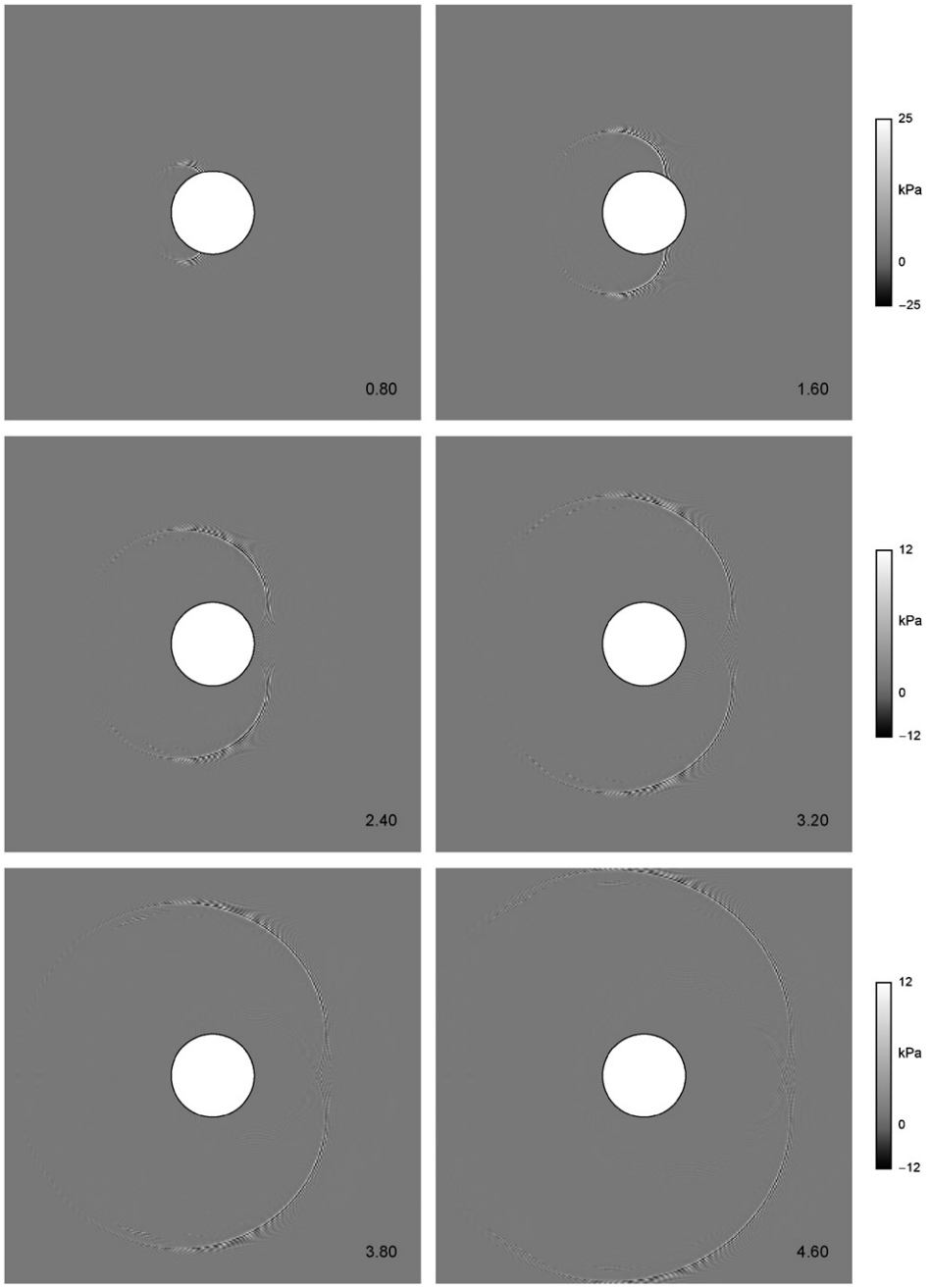

Fig. 16. Difference between the full elastic (bending stiffness taken into account) and membrane (bending stiffness neglected) models, $h_0/r_0 = 0.01$.

perfectly matches that of the experimentally observed one. Thus, it appears that neglecting the bending stiffness is equivalent to eliminating the A_0 wave, and such elimination appears to be a very convenient way of separating the two types of shell-induced waves. We note that since the speed of the circumferential propagation of the S_0 wave does not depend on the shell thickness, and is only determined by the acoustic speed in the shell material, its shape would be exactly the same for a different thickness-to-radius ratio (as long as the surrounding fluid remains the same, of course), although the magnitude would not. As an example, the case of $h_0/r_0 = 0.03$ is shown in Fig. 20(b); the similarity of the shapes of the S_0 waves is apparent. We also note that the excellent agreement between the geometry of the simulated S_0

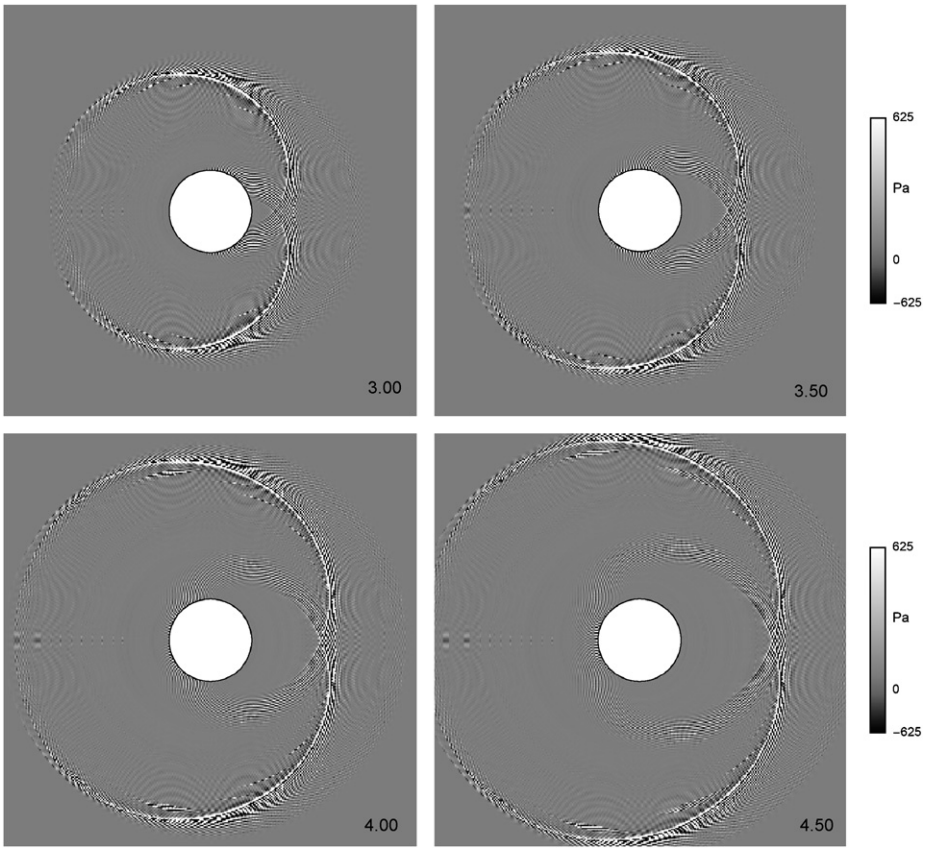

Fig. 17. Close-up of the difference between the full elastic (bending stiffness taken into account) and membrane (bending stiffness neglected) models, $h_0/r_0 = 0.01$, late interaction.

wave and that of the experimentally observed one is yet another indication of the physical adequacy of the model employed, and one more argument in favour of its use to simulate more complex, multi-shell systems.

5. Response functions

The 'volume' response functions $\xi_n^e(r,t)$ are a two-dimensional generalization of the well-known 'surface' (one-dimensional) response functions $\psi_n^e(t)$. The latter were introduced by Geers (1969) in a slightly different form, and a different notation was used. An analytical approach to the inversion of the Laplace transforms of the functions was outlined in that work as well. Since the Laplace transforms of the functions we are interested in, ξ_n^e, only differ from those of ψ_n^e by a parameter r in the numerator (Eqs. (21) and (22) of Part I), it is reasonable to expect that the same approach will be efficient in the present case as well. We therefore apply the inversion procedure developed by Geers (1969) to the Laplace transforms Ξ_n^e, and modify it to account for the difference brought in by the parameter r.

The procedure is based on the use of Cauchy's residue theorem to evaluate Mellin's integral for the functions ξ_n^e,

$$\xi_n^e(r,t) = \frac{1}{2\pi \mathrm{i}} \int_{\varepsilon-\mathrm{i}\infty}^{\varepsilon+\mathrm{i}\infty} \Xi_n^e(r,s)\, \mathrm{e}^{st}\, \mathrm{d}s, \tag{2}$$

where all the singular points of the integrand lie in the half-plane $\mathrm{Re}(s) < \varepsilon$. The procedure involves using Jordan's lemma, so we start with the evaluation of Ξ_n^e at large s. Specifically, it can be shown using the asymptotic expansions for the functions K_n and K_n' (Abramowitz and Stegun, 1965) that

$$\Xi_n^e(r,s) \sim \frac{1}{s\sqrt{r}}\, \mathrm{e}^{s(1-r)}, \quad |s| \gg 1. \tag{3}$$

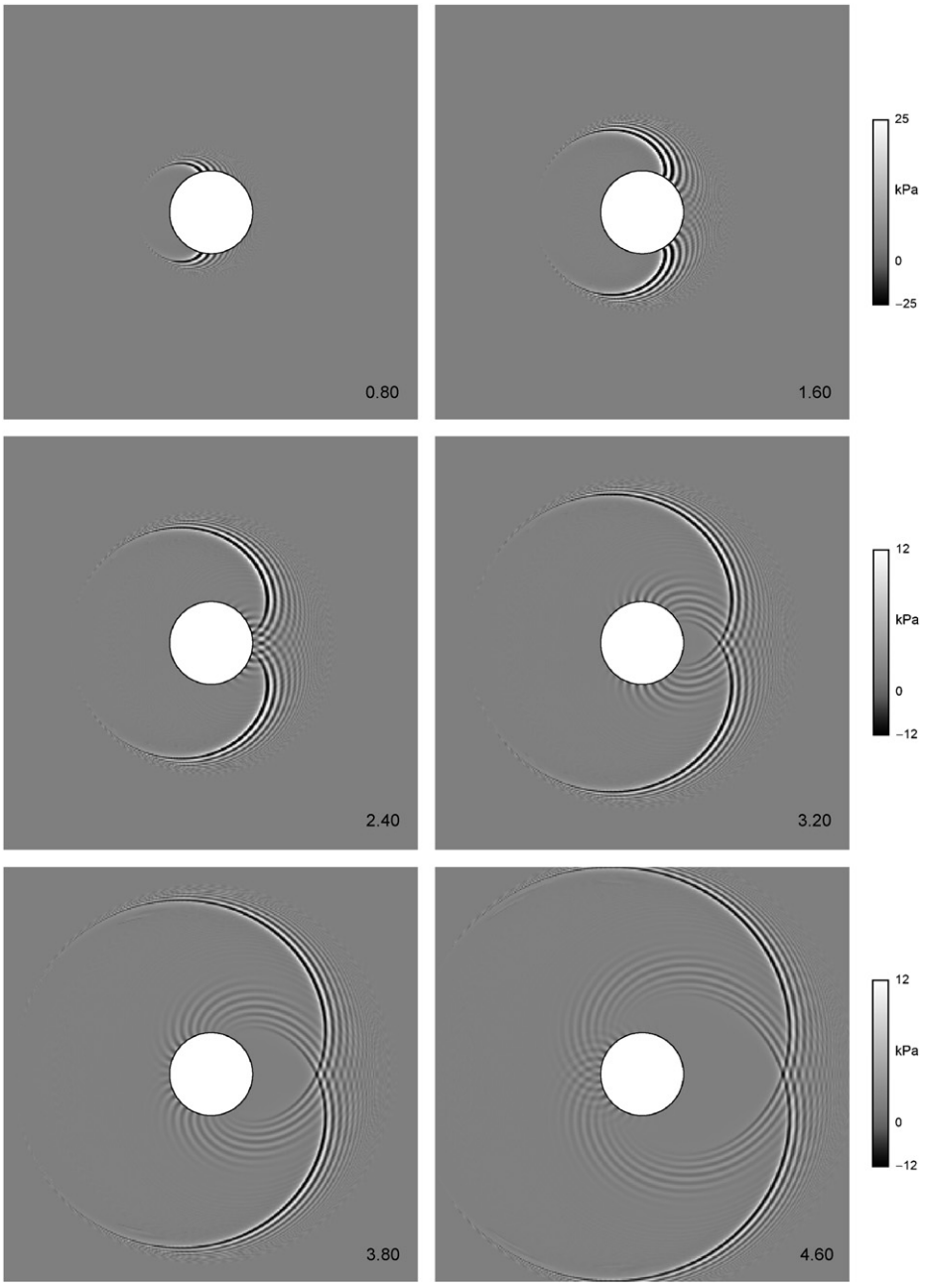

Fig. 18. Difference between the full elastic (bending stiffness taken into account) and membrane (bending stiffness neglected) models, $h_0/r_0 = 0.03$.

Hence, Ξ_n^e do not satisfy Jordan's lemma for any $r>1$. Moreover, if $\mathrm{Im}\, s = 0$ and $\mathrm{Re}\,(s)<0$, for any $r>1$

$$|\Xi_n^e(r,s)| \to \infty \quad \text{as} \quad |s| \to \infty. \tag{4}$$

Such behaviour is a serious obstacle when one intends to use the residue theory for integral evaluation. We therefore consider the modified response functions $\xi_n^*(r,t)$ defined so that their Laplace transforms are

$$\Xi_n^*(r,s) = \Xi_n^e(r,s)\,\mathrm{e}^{s(r-1)} = -\frac{\mathrm{K}_n(rs)}{s\mathrm{K}_n'(s)}\mathrm{e}^{s(r-1)}. \tag{5}$$

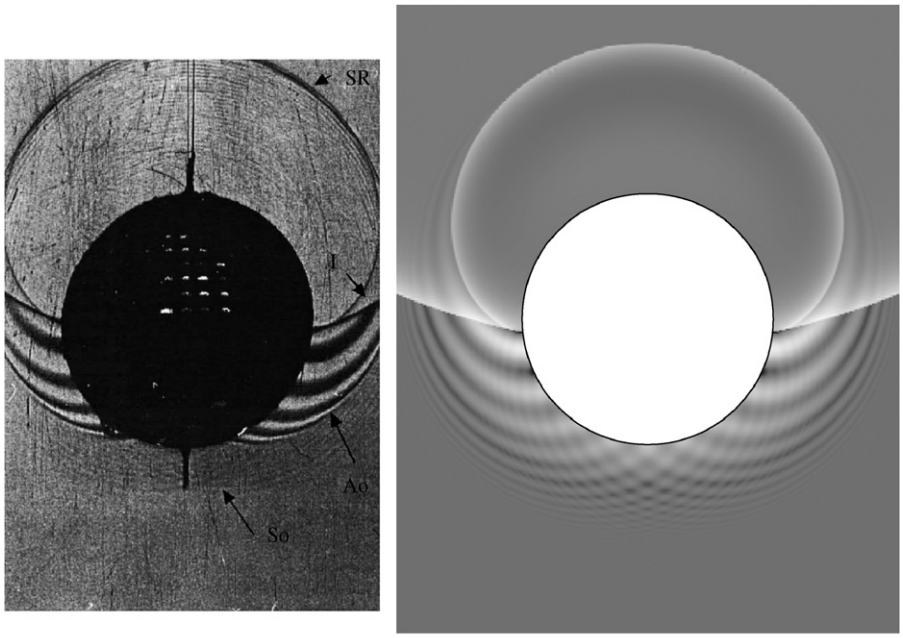

Fig. 19. Comparison of an experimental shadowgraph showing the acoustic field induced by a short pulse incident on a shell with $h_0/r_0 = 0.06$, $t = 1.20$, (a), to the numerically simulated field around the shell with the same thickness-to-radius ratio using the complete elastic model (bending stiffness taken into account), (b) [Shadowgraph (a) is reprinted with permission from Ahyi et al. (1998), Figure 6 (a), ©American Institute of Physics].

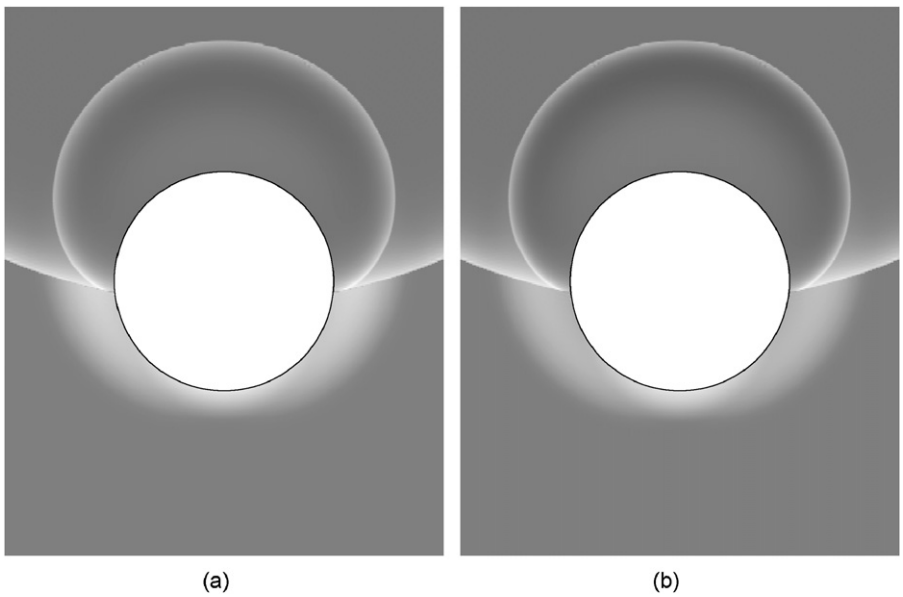

Fig. 20. Numerically simulated fields around shells of two different thicknesses subjected to the same pulse as in Fig. 19(b); $h_0/r_0 = 0.06$, (a), and $h_0/r_0 = 0.03$, (b); simulations are carried out using the membrane model (bending stiffness neglected).

The transforms $\Xi_n^*(r,s)$ satisfy Jordan's lemma since

$$\Xi_n^*(r,t)\sim\frac{1}{s\sqrt{r}},\quad |s|\gg 1. \tag{6}$$

We shall obtain the inverses of Ξ_n^* first, and then the functions ξ_n^e are easily arrived at using the translation theorem

$$\xi_n^e(r,t)=\xi_n^*(r,t-r+1)\mathrm{H}(t-r+1), \tag{7}$$

where H is the Heaviside unit step function. We shall also demonstrate that even though using the modified response functions was prompted by completely mathematical considerations, the resulting translation (and, consequently, the existence of intervals where ξ_n^e is zero) agrees perfectly with the physics of the problem.

We also note that if $r=1$,

$$\Xi_n^e(1,s)\sim\frac{1}{s\sqrt{r}},\quad |s|\gg 1, \tag{8}$$

and $\Xi_n^e(1,s)$ itself satisfy Jordan's lemma. Hence, for $r=1$ there is no need to introduce another function, and one is able to deal with $\Xi_n^e(1,s)$ directly.

Mellin's integral for the functions ξ_n^* is

$$\xi_n^*(r,t)=\frac{1}{2\pi\mathrm{i}}\int_{\varepsilon-\mathrm{i}\infty}^{\varepsilon+\mathrm{i}\infty}\Xi_n^*(r,s)\,\mathrm{e}^{st}\,\mathrm{d}s, \tag{9}$$

and we use Cauchy's residue theorem to evaluate it.

The functions $\mathrm{K}_n(s)$, except for $\mathrm{K}_0(s)$, have a finite number ($N=n$ for even n, and $N=n+1$ for odd n) of complex first order zeros s_k^n, as well as a branch point at $s=0$ for all n. Hence, the functions Ξ_n^* have N simple poles. Since the real parts of all the zeros s_k^n are negative (Abramowitz and Stegun, 1965), the parameter ε in (9) can be any positive number. To evaluate the integral (9), we consider the integration contour Γ shown in Fig. 21 consisting of an arc γ of a circle of a small radius r_γ, two arcs Γ_1 and Γ_2 of a circle of a large radius R_γ, two branch cuts L_1 and L_2, and a segment S of a vertical line $\mathrm{Re}\,(s)=\varepsilon$ (Geers, 1969). It is assumed that all the zeros of ξ_n^* lie inside the domain bounded by Γ.

The approximate distribution of the zeros of K_n' can be obtained (Abramowitz and Stegun, 1965) using the asymptotic formulae for the zeros of the derivatives of the Hankel functions H_n^1. Then, a numerical algorithm (Newton's method in the present work) can be employed to compute the zeros accurately using the approximate values as the starting points. N zeros, where N is always even, are comprised of $N/2$ pairs symmetric about the real axis, and all the zeros are located within the rectangle

$$-n\leqslant\mathrm{Im}(s)\leqslant n, \tag{10}$$

$$-an\leqslant\mathrm{Re}(s)\leqslant 0, \tag{11}$$

where $a\approx 0.66274$ (Abramowitz and Stegun, 1965). A typical distribution of the zeros is shown in Fig. 22.

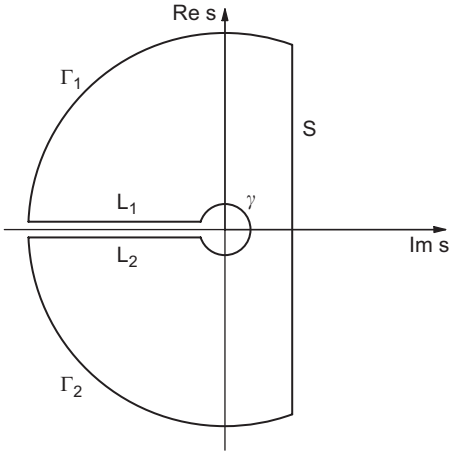

Fig. 21. Integration contour Γ.

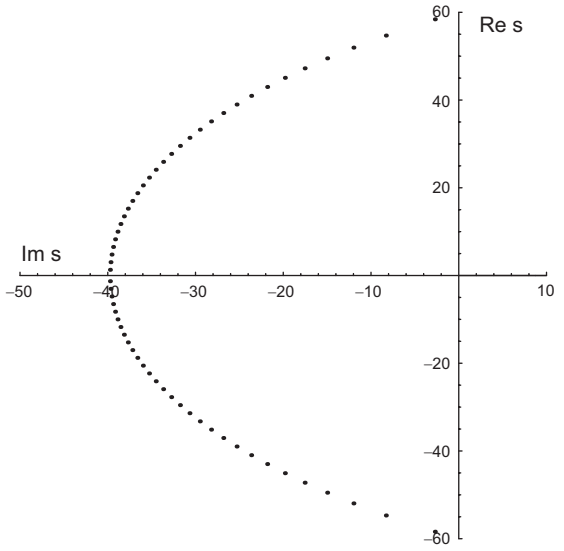

Fig. 22. Zeros of $\mathrm{K}'_{60}(s)$.

Applying the residue theorem to the contour Γ we have

$$\int_{\Gamma}[*]=\int_{\gamma}[*]+\int_{\Gamma_1}[*]+\int_{\Gamma_2}[*]+\int_{L_1}[*]+\int_{L_2}[*]+\int_{S}[*]=2\pi\mathrm{i}\sum_{k=1}^{N}R_k^n, \tag{12}$$

where $[*]=\Xi_n^*(r,s)\,\mathrm{e}^{st}\,\mathrm{d}s$, and R_k^n are the residues of $\Xi_n^*(r,s)\,\mathrm{e}^{st}$ at the poles s_k^n.

We first consider the integral along the arc γ and assume that $r_\gamma \ll 1$. Using the asymptotic expansions for K_n at small s (Abramowitz and Stegun, 1965) it can be demonstrated that

$$\Xi_n^*(r,s)\sim\frac{1}{nr^n},\quad |s|\ll 1, \tag{13}$$

and then it easily follows that

$$\int_{\gamma}[*]\to 0\quad\text{as}\quad r_\gamma\to 0. \tag{14}$$

Since $\Xi_n^*(r,s)$ satisfies Jordan's lemma, we have for the integrals along Γ_1 and Γ_2

$$\int_{\Gamma_1}[*]\to 0\quad\text{when}\quad R_\gamma\to\infty \tag{15}$$

and

$$\int_{\Gamma_2}[*]\to 0\quad\text{when}\quad R_\gamma\to\infty. \tag{16}$$

Computing the integrals along the branch cuts we assume that $z=\eta\mathrm{e}^{\mathrm{i}\pi}$ and $\eta\mathrm{e}^{-\mathrm{i}\pi}$ for the upper (L_1) and lower (L_2) cuts, respectively. Then, it can be shown that when $R_\gamma\to\infty$ and $r_\gamma\to 0$

$$\int_{L_1}[*]+\int_{L_2}[*]\to\Im=-2\pi\mathrm{i}(-1)^n\int_0^\infty\frac{\{\mathrm{I}_n(r\eta)\tilde{\mathrm{K}}_n(\eta)+\mathrm{K}_n(r\eta)\tilde{\mathrm{I}}_n(\eta)\}}{\eta\{\tilde{\mathrm{K}}_n^2(\eta)+\pi^2\tilde{\mathrm{I}}_n^2(\eta)\}}\,\mathrm{e}^{-\alpha\eta}\,\mathrm{d}\eta, \tag{17}$$

where

$$\tilde{\mathrm{K}}_n(\eta)=\mathrm{K}_{n-1}(\eta)+\frac{n}{\eta}\,\mathrm{K}_n(\eta),\quad \tilde{\mathrm{I}}_n(\eta)=\mathrm{I}_{n-1}(\eta)-\frac{n}{\eta}\,\mathrm{I}_n(\eta), \tag{18}$$

and $\alpha = t + r - 1$. Finally,

$$\int_S [*] \to \int_{\varepsilon - \mathrm{i}\infty}^{\varepsilon + \mathrm{i}\infty} \Xi_n^*(r,s)\, \mathrm{e}^{st}\, \mathrm{d}s \quad \text{when} \quad R_\gamma \to \infty. \tag{19}$$

Then, if we consider (12) as $R_\gamma \to \infty$ and $r_\gamma \to 0$, we can write it as

$$\mathfrak{I} + \int_{\varepsilon - \mathrm{i}\infty}^{\varepsilon + \mathrm{i}\infty} \Xi_n^*(r,s)\, \mathrm{e}^{st}\, \mathrm{d}s = 2\pi\mathrm{i} \sum_{k=1}^{N} R_k^n \tag{20}$$

and, comparing (20) and (9), we obtain ξ_n^* as

$$\xi_n^*(r,t) = \sum_{k=1}^{N} R_k^n + (-1)^n \int_0^\infty \frac{\{\mathrm{I}_n(r\eta)\tilde{\mathrm{K}}_n(\eta) + \mathrm{K}_n(r\eta)\tilde{\mathrm{I}}_n(\eta)\}}{\eta\{\tilde{\mathrm{K}}_n^2(\eta) + \pi^2\tilde{\mathrm{I}}_n^2(\eta)\}}\, \mathrm{e}^{-\alpha\eta}\, \mathrm{d}\eta, \tag{21}$$

where the residue term is absent for $n = 0$. The residues R_k^n at the poles s_k^n can be shown to be

$$R_k^n = -\frac{\mathrm{K}_n(rs_k^n)}{\mathrm{K}_n(s_k^n)} \frac{s_k^n}{\{(s_k^n)^2 + n^2\}}\, \mathrm{e}^{s_k^n t}, \tag{22}$$

and hence

$$\xi_n^*(r,t) = -\sum_{k=1}^{N} \frac{\mathrm{K}_n(rs_k^n)}{\mathrm{K}_n(s_k^n)} \frac{s_k^n}{\{(s_k^n)^2 + n^2\}}\, \mathrm{e}^{s_k^n t} \tag{23}$$

$$+ (-1)^n \int_0^\infty \frac{\{\mathrm{I}_n(r\eta)\tilde{\mathrm{K}}_n(\eta) + \mathrm{K}_n(r\eta)\tilde{\mathrm{I}}_n(\eta)\}}{\eta\{\tilde{\mathrm{K}}_n^2(\eta) + \pi^2\tilde{\mathrm{I}}_n^2(\eta)\}}\, \mathrm{e}^{-\alpha\eta}\, \mathrm{d}\eta, \quad n \geqslant 1 \tag{24}$$

and

$$\xi_0^*(r,t) = \int_0^\infty \frac{\{\mathrm{I}_0(r\eta)\mathrm{K}_1(\eta) + \mathrm{K}_0(r\eta)\mathrm{I}_1(\eta)\}}{\eta\{\mathrm{K}_1^2(\eta) + \pi^2\mathrm{I}_1^2(\eta)\}}\, \mathrm{e}^{-\alpha\eta}\, \mathrm{d}\eta. \tag{25}$$

Taking into account the symmetry of the zeros of K_n', i.e. the fact that s_k^n, $k = 1, \ldots, N$ can be represented as

$$s_m^n = a_m \pm \mathrm{i}b_m, \quad m = 1, \ldots, N^*, \tag{26}$$

where $N^* = N/2$ and a_m and b_m are real, the residual term in (24) can be easily written in a from that only includes real numbers.

The equations derived appear to be quite attractive from the computational point of view. Indeed, for small n Eq. (24) works very efficiently for any t. Unfortunately, for larger n there exists an interval $[0, t_c]$ where (24) produces catastrophic cancellation. The situation is worsened by the fact that the length of this interval increases with r. For example, for $n = 100$ and $r = 2$ the interval prone to catastrophic cancellation is estimated to be $[0, 0.002]$, and for the same n but $r = 5$ the values of t as large as $t = 0.30$ could produce catastrophic cancellation. For $n = 140$ and $r = 2$ the interval in question is $[0, 0.12]$, and for $n = 140$ and $r = 5$ it is $[0, 0.40]$. If catastrophic cancellation does occur, the accuracy of computations required is such that using (24) becomes impractical. Hence, a different approach had to be developed to compute ξ_n^* in the problem areas.

The alternative approach we chose here is based on the idea introduced by Dubner and Abate (1968). Namely, instead of dealing with Mellin's integral directly, it is reduced to the Fourier cosine transform of the real part of Ξ_n^*

$$\xi_n^* = \frac{2\mathrm{e}^{at}}{\pi} \int_0^\infty \mathrm{Re}\, \{\Xi_n^*(r,s)\} \cos\omega t\, \mathrm{d}\omega, \tag{27}$$

where $s = a + \mathrm{i}\omega$ and $a > 0$, and is evaluated numerically. The integration step size, value of the parameter a, and the number of terms used in the truncated series were chosen to ensure an acceptably accurate result for any r, n, and t of interest. We note that such an approach to the inversion has no restrictions on the value of t, and, therefore, it alone is sufficient to compute ξ_n^*.

Using the methodology outlined, the functions ξ_n^* were computed. Then, the translation (7) was applied, and the functions ξ_n^e were computed as well. As we mentioned, the translation has a clear physical interpretation in the present case. Namely, the fact that

$$\xi_n^e(r,t) = 0 \quad \text{for all} \quad t < r - 1 \tag{28}$$

reflects the fact that a 'signal' induced by the moving shell surface at $t = 0$ does not reach the layer (r, θ), $\theta \in [-\pi, \pi]$ of the external fluid until the instant $t = r - 1$ (at $t = 0$ the 'signal' starts to travel from the shell surface where $r = 1$). Thus, as it was the case when the internal fluid was considered (Iakovlev, 2006), the mathematical nature of the response functions clearly reflects the most essential physical features of the interaction. However, it is rather obvious that, for the absence of the multiple reflection and focusing, the physics of the external acoustic field is considerably less complex than that of the internal one, and the same is expected to be the case for the response functions.

Figs. 23 and 24 show several response functions computed for various n and r. First of all, we notice that the functions ξ_n^e have no singularities and only one finite discontinuity—a mathematical representation of the fact that no reflection and/or focusing of acoustic waves radiated by the shell surface occur in the external fluid. The only finite discontinuity occurs at $t = r - 1$, the dimensionless time that corresponds to the instant when the acoustic wave induced by the shell surface arrives at the point (r, θ). Unlike it was the case with the internal response functions, the value of ξ_n^e at the point of discontinuity is $r^{-0.5}$, and not a half of the sum of the left- and right-side limits (note that ξ_n^e are shown in Figs. 23 and 24 as continuous). After the shell-radiated wave passes the point (r, θ), the point never experiences sudden changes of pressure again, and thus the response functions are continuous for any $t > r - 1$. We have therefore

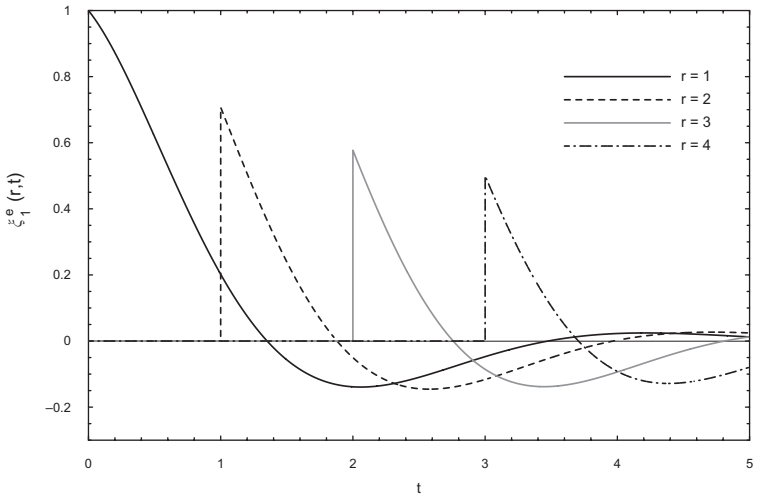

Fig. 23. Function $\xi_1^e(r, t)$ for various r.

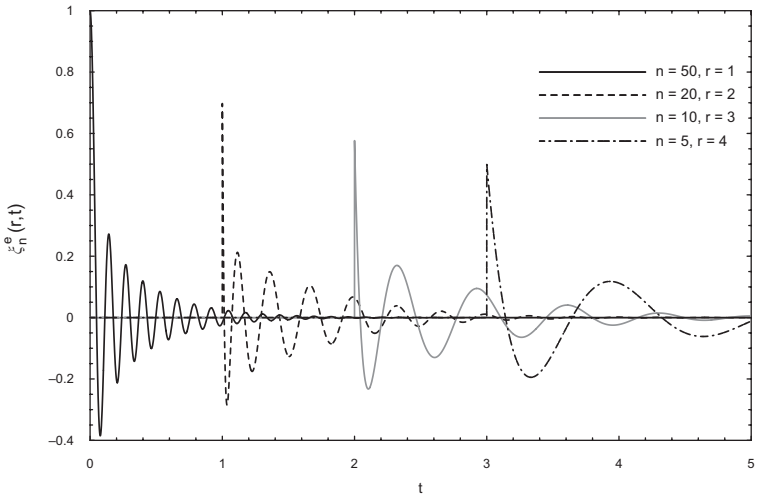

Fig. 24. Function $\xi_n^e(r, t)$ for various n and r.

demonstrated that, indeed, the response functions ξ_n^e are incomparably less complex than their 'internal' counterparts ξ_n^i (Iakovlev, 2006), even though one still faces a number of computational challenges dealing with them. For the same r and increasing n, the location of the point of discontinuity remains the same for all n, but the frequency of the oscillations in the non-zero region increases, much like it was the case for the 'surface' external response functions ψ_n^e (Iakovlev, 2004).

6. Conclusions

The interaction between a submerged evacuated cylindrical shell and an external shock wave was considered. The numerical analysis of the solution obtained in Part I was carried out. Several other issues of interest were addressed as well.

The convergence of the series for the normal displacement, strain, and pressure was analysed. The latter was analysed both on the shell surface and inside the fluid domain, and it was shown that the maximum error due to series truncation is reached inside the fluid, quite far away from the shell surface. It was also established that the convergence is the best for the displacement series, followed by the series for the strain (in both cases, as few as 10 terms provide acceptably accurate results). The pressure series exhibits the worst convergence, and sometimes as many as 300 terms are needed to be taken into account to ensure physically adequate appearance of simulated acoustic fields. If realistic visualization is not a priority, 150 terms will ensure acceptably accurate results almost everywhere in the fluid domain of interest.

The convergence analysis was summarized in a table showing the evolution of the error as the number of terms retained in the respective series changed. Both the head and tail points were considered, and it was found that the convergence of the displacement, strain, and total pressure is very similar at both points. The diffraction and radiation pressure appear to exhibit different convergence at the head and tail points. It was also noticed that the radiation pressure converges much better than the diffraction one, and thus the overall convergence of the total pressure appears to be determined by the convergence of the diffraction one.

The convergence of the finite-difference scheme used to obtain the displacements was addressed as well. It was established that the step size needs to be quite small for the scheme to converge, particularly when the bending stiffness is taken into account (in which case any step size above 0.002 will cause the scheme to diverge). In spite of that, it was demonstrated that when the step size is reduced to about 0.001 or less, the scheme starts to rapidly converge for both shell deformation models, and further decrease of the step size leads to a very insignificant (less than 1%) change in the displacements.

A number of one-dimensional plots of the normal displacement, strain, and pressure were included as well, aiming at a potential use as benchmarks for verification of numerical codes. The numerical imperfections (due to series convergence) were retained in the plots to illustrate the limitations of the model used; however, the pressure was the only variable for which such imperfections were a concern. Even in that case, the presence of the 'convergence noise' in the plots did not appear to be a serious limiting factor since it is highest in the regions where the pressure is known to be zero.

The effect of the bending stiffness on the acoustic field was addressed as well. It was established that for a very thin shell ($h_0/r_0 \leqslant 0.01$), the contribution of the bending stiffness is limited to very narrow regions behind the front of the incident (the primary component) and scattered (secondary component) waves. For thicker shells, the contribution of the bending stiffness is much less localized, and has a considerably more significant effect on the total acoustic field; the secondary component is much more pronounced as well. It thus appears that, as far as the acoustic field is concerned, the bending stiffness manifests itself at the points of contact between the shell and incident and scattered waves, and does not seem to have any effect on the acoustic field induced by the elastic waves propagating in the shell.

The magnitude of the 'bending-stiffness-induced' waves does not appear to depend on the shell thickness considerably; their frequency, however, certainly does, and it significantly decreases with thickness. These observations further support the conclusions made earlier (Iakovlev, 2007) about the importance of taking the bending stiffness into account for shells with the thicknesses-to-radius ratio exceeding 0.01. It was also observed that the membrane model only reproduces one of the two shell-radiated waves observed in the experiments, namely the symmetric Lamb wave S_0, and not the antisymmetric wave A_0. The model with the bending stiffness, however, produces a mixed radiated field that is neither S_0 nor A_0 waves, the aspect of the shell–shock interaction modelling that definitely deserves further investigation.

Complementing the findings of Part I, further comparison to experimental images was carried out, this time with the focus on the shell-induced field. The linear membrane model was shown to produce an excellent agreement with experiments as far as the S_0 wave is concerned. This reinforces the point made earlier regarding the suitability of the

solution developed here and in the author's previous work (Iakovlev, 2006, 2007) for analysis of the shell–shock interaction when the incident load is either a weak shock wave or an acoustic pulse. The good agreement with the experiments in terms of the shell-induced waves is particularly comforting since such waves are secondary in magnitude, and thus represent a more subtle feature of the interaction.

The dynamics of the total diffracted–radiated field for the membrane model of the shell (bending stiffness neglected) was represented by a number of snapshots, and those, in combination with the images of Part I for an absolutely rigid cylinder and fully elastic shell (bending stiffness taken into account), offer one an opportunity to analyse the evolution of the acoustic field when the elastic properties of the shell change from the absolutely rigid state to the membrane one.

The response functions of the problem were studied in detail as well. A procedure aimed at an efficient and accurate computation of the functions was developed, and the disadvantages of a purely analytical approach were outlined. The functions considered here are a two-dimensional ('volume') generalization of the one-dimensional ('surface') response functions that have been used, in various forms, for several decades to analyse both the stress–strain states of shock-interacting shells and the surface distribution of the pressure induced by such interaction.

The results presented here complement Part I, and thus complete the fully linear study of an empty circular cylindrical shell subjected to a plane or cylindrical shock wave. In terms of the bigger picture of the research initiatives undertaken by the author, the present work completes the preparations necessary before the most interesting (as far as a single-shell system is concerned) problem of the interaction between a shock wave and a shell filled with and submerged into fluids with different properties can be approached. Considering the good overall agreement with experiments seen for both internal and external acoustic fields, the approach developed appears to be quite promising for analysis of more complex shell systems as well.

Acknowledgements

The author gratefully acknowledges the financial support of the Natural Sciences and Engineering Research Council (NSERC) of Canada (Discovery Grant 261949), the Killam Trusts, and the Faculty of Engineering, Dalhousie University. The author is also grateful to Dr Ayayi Claude Ahyi of the Auburn University, Alabama, USA, for granting a permission to reproduce photographs from one of his publications, and for sharing a previously unpublished experimental image that was helpful in validating some of the numerical simulations presented in this paper. Last but not least, the author thanks Ryan Barnes, a Mechanical Engineering student at Dalhousie University, for his dedicated assistance with often challenging numerical analysis that ensured the accuracy of the results presented.

References

Abramowitz, M., Stegun, I.A., 1965. Handbook of Mathematical Functions. Dover Publications, New York.

Ahyi, A.C., 2006. Personal communication.

Ahyi, A.C., Pernod, P., Gatti, O., Latard, V., Merlen, A., Uberall, H., 1998. Experimental demonstration of the pseudo-Rayleigh (A_0) wave. Journal of the Acoustical Society of America 104, 2727–2732.

Dubner, H., Abate, J., 1968. Numerical inversion of Laplace transforms by relating them to the finite Fourier cosine transform. Journal of the Association for Computing Machinery 15, 115–123.

Geers, T.L., 1969. Excitation of an elastic cylindrical shell by a transient acoustic wave. Journal of Applied Mechanics 36, 459–469.

Iakovlev, S., 2004. Influence of a rigid co-axial core on the stress–strain state of a submerged fluid-filled circular cylindrical shell subjected to a shock wave. Journal of Fluids and Structures 19, 957–984.

Iakovlev, S., 2006. External shock loading on a submerged fluid-filled cylindrical shell. Journal of Fluids and Structures 22, 997–1028.

Iakovlev, S., 2007. Submerged fluid-filled cylindrical shell subjected to a shock wave: fluid–structure interaction effects. Journal of Fluids and Structures 23, 117–142.

Zhang, P., Geers, T.L., 1993. Excitation of a fluid-filled, submerged spherical shell by a transient acoustic wave. Journal of the Acoustical Society of America 93, 696–705.